NEAR-FIELD MIMO-SAR MILLIMETER-WAVE IMAGING

by

Muhammet Emin Yanik

APPROVED BY SUPERVISORY COMMITTEE:

Murat Torlak, Chair

Kenneth O

Naofal Al-Dhahir

Andrew Blanchard

*Dedicated to my family.*

# NEAR-FIELD MIMO-SAR MILLIMETER-WAVE IMAGING

by

MUHAMMET EMIN YANIK, BS, MS

DISSERTATION PROPOSAL

Presented to the Faculty of

The University of Texas at Dallas

in Partial Fulfillment

of the Requirements

for the Degree of

DOCTOR OF PHILOSOPHY IN

ELECTRICAL AND COMPUTER ENGINEERING

THE UNIVERSITY OF TEXAS AT DALLAS

December 2019

# ACKNOWLEDGMENTS

Foremost, I would like to express my sincere thanks to my advisor, Professor Murat Torlak, for being a great mentor to me since the beginning of my journey at the University of Texas at Dallas. He always inspired me to grow academically and encouraged me to maintain my confidence to achieve our goals. Much of my success has come from his patience, enthusiasm, motivation, and immense knowledge of the subject. He is always kind in his way of guiding and teaching. It has been a great pleasure working with him.

Besides my advisor, I am grateful to my dissertation committee members, Professor Naofal Al-Dhahir, Professor Kenneth O, and Professor Andrew Blanchard for their precious time and valuable suggestions.

I would like to thank Dr. Dan Wang, Dr. Adeel Ahmad, and my other colleagues at Texas Instruments for their contributions to this research. Many thanks to my labmates at the Wireless Information Systems Laboratory and the Texas Analog Center of Excellence, for their friendship throughout these years and for the hours we have spent together discussing valuable ideas as a team. I am also thankful to the Semiconductor Research Corporation (SRC) and the National Science Foundation (NSF) for supporting my research.

I would express my gratitude toward my parents, my sisters, my brother, and my relatives for their unconditional support during my entire life, and for all the things they have given me.

The last but the not least, I am in indebted to my wife, my love, and my soulmate Gaye Yanik, for her endless support during tough times. She is the source of power for me to overcome all the challenges that I have faced.

April 2019

NEAR-FIELD MIMO-SAR MILLIMETER-WAVE IMAGING

Muhammet Emin Yanik, PhD
The University of Texas at Dallas, 2019

Supervising Professor: Murat Torlak, Chair

There is a strong desire to exploit the progress in complementary metal-oxide semiconductor (CMOS) based millimeter-wave (mmWave) sensors in wide range of imaging applications including medical, automotive, and security. The primary challenge of a cost-effective and low-complexity near-field mmWave imaging system is to achieve high-resolution with as few antenna elements as possible. Multiple-input multiple-output (MIMO) radar using simultaneous operation of spatially diverse transmit and receive antennas is a good candidate to increase the number of available degrees of freedom. On the other hand, higher integration complexity of extremely dense transceiver electronics limits the use of MIMO only solutions within a relatively large imaging aperture. Hybrid concepts combining synthetic aperture radar (SAR) techniques and MIMO arrays present a good compromise to achieve short data acquisition time and low-complexity. However, compared with conventional monostatic sampling schemes, image reconstruction methods for MIMO-SAR are more complicated. This dissertation proposal presents a high-resolution mmWave imaging system combining two-dimensional (2-D) MIMO arrays with SAR, along with novel Fourier based image reconstruction algorithms. The proposed algorithms are verified by both simulation and real data collected with our mmWave imager prototype utilizing commercially available MIMO radar sensors. The experimental results confirm that our complete solution presents a strong potential in high-resolution imaging with a significantly reduced number of antenna elements.

TABLE OF CONTENTS

LIST OF FIGURES

LIST OF TABLES

# CHAPTER 1

# INTRODUCTION

## 1.1 Background and Motivation

Millimeter-wave (mmWave) imaging technology has gained significant attention in recent years and it now plays an important role in many applications including medical diagnostics [1, 2, 3], security screening [4, 5, 6, 7, 8, 9], and structure inspection [10]. The major challenges of building mmWave imaging systems are the cost and complexity arising from the need for a large number of transceiver elements.

The cross-range image resolution and the spatial sampling criteria are two key system parameters that determine the required number of antennas. While the range resolution is directly related to the bandwidth of the transmitting signal, the cross-range resolution is also determined by the effective length of the radar aperture. For example, an effective aperture size of 50 wavelengths ($\lambda$) along both horizontal and vertical directions is needed to achieve a 5 mm resolution in both axes at 50 cm range [4, 5]. On the other hand, $\lambda/4$ spacing is necessary between the measurement points to prevent the formation of unwanted imaging artifacts in a near-field scenario [4]. Hence, in order to satisfy the above mentioned image resolution under the required spatial sampling criteria, an ideal imaging system would consist of a two-dimensional (2-D) array with approximately 40000 antenna elements.

In recent years, great progress has been made in the semiconductor technology to enable cost-effective sensor solutions. Complementary metal-oxide semiconductor (CMOS) based frequency-modulated continuous-wave (FMCW) mmWave radars integrate all the analog and radio-frequency (RF) functionality as well as the low-level signal processing capability into a single chip with a compact form factor [11]. Such a highly integrated device enables the mmWave radar systems to be cost-effective and miniaturized. However, implementing densely placed transceivers required for high-resolution imaging is still a challenging effort.

A well-known approach to mitigate this challenge is the realization of multiple-input multiple-output (MIMO) array topologies [12, 13, 14]. Fully electronic multistatic sampling of large radar apertures using MIMO arrays has been incorporated into various near-field imaging systems [6, 15, 16]. While real-time operation is an ultimate goal for many applications, higher hardware complexity of integrating a large number of transceiver antennas makes fully electronic sampling less likely to be widely deployed. As a result, using a hybrid concept based on the combination of synthetic aperture radar (SAR) technique [17, 18] and MIMO array leads to lower hardware complexity than fully electronic sampling solutions [5, 19].

### 1.2 Research Objectives and Previous Work

The main objective of this dissertation proposal refers to a novel combination of commercially available system-on-chip MIMO radar sensors and SAR to offer a cost-effective and practical mmWave imaging solution with high-resolution capability. To achieve this goal, the primary focus of our research is the employment of computationally efficient image reconstruction algorithms for MIMO-SAR configurations, which remains a challenge in near-field imaging applications.

In near-field, the plane-wave assumption is invalid and the spherical electromagnetic wave model has to be used. The image reconstruction process must be able to completely compensate for the curvature of the wavefront. Although the time-domain correlation (or backprojection) method [5, 20], which provides a straightforward solution to estimate target area reflectivity by correlating the recorded data with the signature of a unit reflector at each spatial coordinate, can be used for any arbitrary multistatic array configuration, it suffers from high computational load.

For monostatic sampling schemes, where the measurements are taken by collocated transmit and receive antennas over regular spatial intervals, near-field image reconstruction has

long been implemented using Fourier based inversion methods for both planar [4, 21, 22] and cylindrical/spherical [23, 24] scanning geometries. Unfortunately, these methods cannot be directly used for multistatic systems due to their need to consider the different trajectories of the incident and reflected electric fields. Therefore, the fast implementation of reconstruction algorithms in multistatic structures is more challenging compared to monostatic systems.

To overcome this challenge, modified wavenumber domain image reconstruction approaches accounting for multistatic array topology along with wavefront curvature in near-field have been presented. A Fourier-based multistatic image reconstruction algorithm for 2-D MIMO proposed in [25] has the requirement of satisfying the Nyquist sampling criteria for both receiver and transmitter arrays. The reconstruction approaches for multistatic imaging in [26] and [19] are only limited to the systems synthesizing the 2-D aperture with one-dimensional (1-D) SAR along with 1-D MIMO sampling.

Such needs limit the use of these algorithms for arbitrary array configurations. Besides, all these techniques involve computationally expensive multidimensional wavenumber space interpolation to map the spectral domain data in nonuniform grids into a uniform one. This process makes these algorithms equally or less efficient than the direct time-domain reconstruction in high throughput applications [5] . Therefore, the common issues concerning the previous works motivate to revise the image reconstruction for a general MIMO-SAR configuration and to improve the computational complexity while keeping the required image quality.

### 1.3 Contributions and Proposed Work

In response to all these major challenging requirements, we propose a complete and novel near-field mmWave imaging solution utilizing sparse MIMO-SAR topology, and achieve the following contributions:

1. We investigate the wavenumber domain of the backscattered data by expanding the study in [27] for MIMO-SAR configuration. We establish the nonlinear relation between the wavenumber spectrum of the backscattered data and the reconstructed image, which, to our knowledge, has not been studied in the previous literature. We analyze the analytical effect of aliasing due to sparse sampling both on the wavenumber and spatial domains. The contribution is based on the following publication:

    - M.E. Yanik and M. Torlak, "Near-field MIMO-SAR millimeter-wave imaging with sparsely sampled aperture data," *IEEE Access*, vol. 7, pp. 31801-31819, Mar. 2019.

2. We then propose an efficient Fourier based imaging algorithm for sparse MIMO-SAR to recover the spectrum of alias-free images by properly combining the overlapped spectrum of sparse subchannels. The proposed image reconstruction algorithm for sparse multistatic sampling is based on the expansion of extremely efficient and interpolation-free Fourier based monostatic SAR imaging. To reconstruct near-field images from spatially diverse transmit and receive antennas, we introduce a multistatic-to-monostatic phase correction approach. Besides, the proposed reconstruction formula compensates the propagation loss, which is typically ignored in existing studies, to improve the imaging quality for the near-field operations. The contribution is founded in the following publication:

    - M.E. Yanik and M. Torlak, "Near-field MIMO-SAR millimeter-wave imaging with sparsely sampled aperture data," *IEEE Access*, vol. 7, pp. 31801-31819, Mar. 2019.

3. To validate the proposed image reconstruction algorithms and to investigate key system parameters such as image resolution and spatial sampling criteria, we build a

mmWave imaging prototype utilizing commercially available MIMO sensors and a custom designed two-axis automatic rail system. We present real imaging results to show the effectiveness of the proposed system that achieves high-resolution imaging performance with a significantly reduced number of antenna elements. Most importantly, to the best of our knowledge, we reconstruct the first MIMO-SAR image in the literature using Texas Instruments' system-on-chip mmWave radar sensors. The contribution is based on the following publications:

- M.E. Yanik and M. Torlak, "Millimeter-wave near-field imaging with two-dimensional SAR data," in *Proc. SRC Techcon*, Austin, Texas, US, Sep. 2018.
- M.E. Yanik and M. Torlak, "Near-field two-dimensional SAR imaging by millimeter-wave radar for concealed item detection," in *IEEE Radio & Wireless Symposium*, Orlando, Florida, US, Jan. 2019.
- M.E. Yanik and M. Torlak, "Near-field MIMO-SAR millimeter-wave imaging with sparsely sampled aperture data," *IEEE Access*, vol. 7, pp. 31801-31819, Mar. 2019.
- M.E. Yanik and M. Torlak, "Development of a Millimeter-Wave Imaging System Using MIMO-SAR Configuration," *IEEE Trans. on Instrumentation and Measurement*, to be submitted.

4. Finally, we will propose a novel and computationally efficient three-dimensional (3-D) image reconstruction technique based on MIMO-SAR geometry. The detailed description of the contribution will be covered in the following publications:

   - M.E. Yanik and M. Torlak, "MIMO-SAR Based 3-D Millimeter-Wave Imaging in Near-Field Applications," in *Proc. SRC Techcon*, Austin, Texas, US, Sep. 2019, abstract submitted.

- M.E. Yanik and M. Torlak, "A Novel 3-D Holographic Millimeter-Wave Imaging Approach Based on MIMO-SAR," *IEEE Trans. on Microwave Theory and Techniques*, to be submitted.

## 1.4 Outline

The rest of the dissertation proposal is organized as follows:

- Chapter 2 presents the proposed MIMO-SAR configuration, and discusses the virtual antenna array concept in near-field using a multistatic-to-monostatic correction factor to improve Fourier based image formation.

- Chapter 3 reviews the standard monostatic SAR image reconstruction framework, which forms the basis of our MIMO-SAR image formation.

- Chapter 4 will address the signal processing steps involved in the proposed sparse MIMO-SAR image reconstruction starting with the wavenumber spectrum analysis of subsampling and its effect on the image domain, followed by the proposed novel image reconstruction technique that is compatible with the sparsely sampled aperture data.

- Chapter 5 presents the hardware architecture of the prototyped imager, proposes a calibration method to compensate the gain and phase mismatches of the MIMO array elements, and discusses the image resolution, which is an important performance metric in imaging.

- Simulations and measurement results are reported in Chapter 6, which is followed by the summary and proposed work in Chapter 7.

# CHAPTER 2

# SYSTEM MODEL

In this dissertation proposal, we synthesize a 2-D SAR aperture by mechanically scanning a MIMO array in a parallel track pattern as shown in Fig. 2.1. In the following sections, we present the geometrical setup for the proposed MIMO-SAR system.

## 2.1 MIMO-SAR Configuration

The radar measurements are performed by moving a MIMO array continuously across $xy$ plane, along parallel lines, as shown in Fig. 2.1. Both SAR and MIMO apertures can be sparse. The unprimed and primed coordinates represent the measurement positions on the scan aperture and image pixel positions over a target aperture, respectively. In the established right-handed $(x, y, z)$ Cartesian coordinate system, $x-$axis, $y-$axis, and $z-$axis denote horizontal, vertical, and depth directions, respectively.

The reference point $(x, y, 0)$ is the position of the MIMO array at a specific measurement instant. The target aperture is at the distance of $z_0$. The image pixel coordinates are given as $(x', y', z_0)$. The target is assumed to be a 2-D object and parallel to the scanning plane.

## 2.2 The Virtual Array Concept

We consider a sparse MIMO array equipped with $M_T$ transmit and $M_R$ receive antenna elements. Let the $u$th transmit and the $v$th receive antennas be located at $\mathbf{r}_u \in \mathbb{R}^3$ and $\mathbf{r}_v \in \mathbb{R}^3$, respectively, as shown in Fig. 2.2a. The transmit and receive antenna locations are characterized by

$$g_T(\mathbf{r}) = \sum_{u=0}^{M_T-1} \delta(\mathbf{r} - \mathbf{r}_u), \quad g_R(\mathbf{r}) = \sum_{v=0}^{M_R-1} \delta(\mathbf{r} - \mathbf{r}_v). \tag{2.1}$$

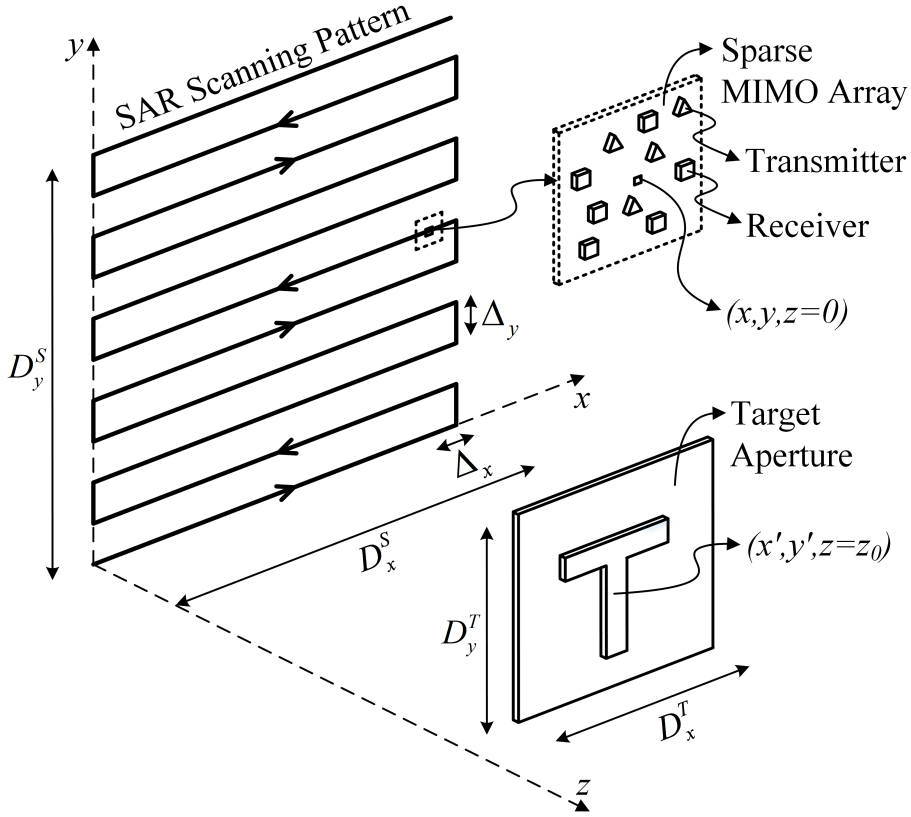


Figure 2.1: Geometry of SAR scanned in a parallel track pattern with a sparse MIMO array.

In a far-field scenario, assume that the distance to the target aperture is much larger than the distance between the transmit and receive elements of the MIMO array. This assumption leads to a conventional midpoint approximation that holds for a small fraction of $\epsilon$ for each $u \in \{1, ..., M_T\}$ and $v \in \{1, ..., M_R\}$ as reported in [28],

$$|\mathbf{r}_u - \mathbf{r}_v| \leq \sqrt{4\epsilon\lambda R}, \tag{2.2}$$

where $\lambda$ is the wavelength and $R$ is the distance from the midpoint of the antennas to the ideal point scatterer. Then the corresponding transceiver antenna pair is approximated by a single monostatic virtual element located at [28, 13, 29]

$$\mathbf{r}_{uv} = (\mathbf{r}_u + \mathbf{r}_v)/2. \tag{2.3}$$

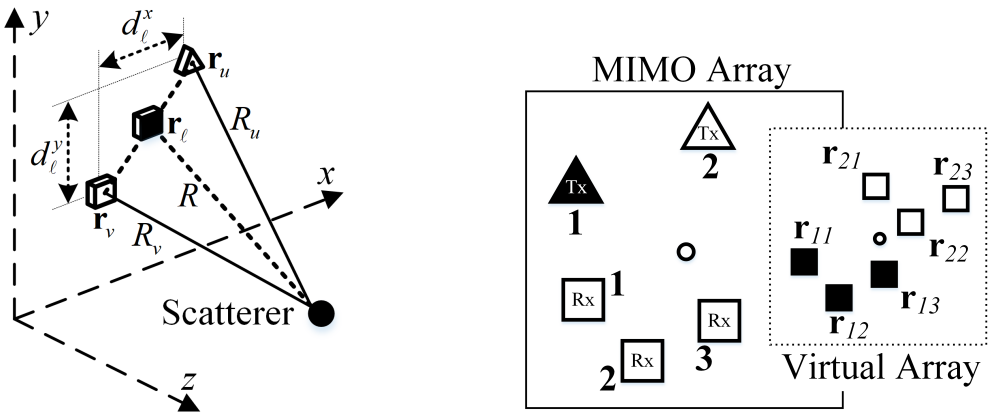


(a) (b)

Figure 2.2: (a) MIMO array in near-field for $u$th transmit and $v$th receive antennas. (b) An example of MIMO array with two transmit and three receive antennas, and corresponding virtual array.

The scaling factor of 1/2 is due to the round-trip propagation. The location of this monostatic virtual element as depicted in Fig. 2.2a is also called equivalent phase center. An example of MIMO array with $M_T = 2$ and $M_R = 3$ antennas and the corresponding virtual array are depicted in Fig. 2.2b. Thus, a MIMO array with $M_T + M_R$ physical antennas can be approximated by a virtual array with $L = M_T \times M_R$ monostatic elements. We can simplify the virtual element subscript as $\ell$, where $\ell \in \{1, ..., L\}$, for simplicity. Then the corresponding distribution function of the virtual array elements can be obtained by performing convolution of the transmitter and receiver element distributions in (2.1) as

$$g_V(\mathbf{r}) = g_T(\mathbf{r}) \circledast g_R(\mathbf{r}) = \sum_{\ell=0}^{L-1} \delta(\mathbf{r} - \mathbf{r}_\ell). \tag{2.4}$$

Therefore, the virtual array, which describes the set of independent monostatic elements that can collect the equivalent data, is half the size of the physical MIMO array (i.e., sum of the transmit and receive array aperture sizes) in each dimension. To create this virtual array architecture, receiver antennas must be able to separate the signals corresponding to

different transmitter antennas. In this dissertation proposal, the orthogonality between the transmit antennas is achieved by employing time division multiplexing (TDM) technique.

### 2.3 The Virtual Array Response in Near-Field Imaging

For near-field imaging applications, small fraction of $\epsilon$ assumption in (2.2) does not hold and an improved approximation is necessary. In the following, we will derive an efficient proper adjustment factor to create an equivalent virtual array from a MIMO array for near-field scenarios.

Let us express the total round-trip distance associated with the $u$th transmitter element at $(x_u, y_u, 0)$ and the $v$th receiver element at $(x_v, y_v, 0)$ to a point scatterer at $(x', y', z_0)$ as

$$\begin{aligned} R_\ell = R_u + R_v = &\sqrt{(x_u - x')^2 + (y_u - y')^2 + z_0^2} \\ &+ \sqrt{(x_v - x')^2 + (y_v - y')^2 + z_0^2}. \end{aligned} \tag{2.5}$$

Let us denote the location of the virtual antenna element corresponding to the $u$th transmitter and the $v$th receiver as $(x, y)$. We can express the $u$th transmitter and the $v$th receiver locations as

$$\begin{aligned} x_u &= x + d_\ell^x/2, \qquad & y_u &= y + d_\ell^y/2, \\ x_v &= x - d_\ell^x/2, \qquad & y_v &= y - d_\ell^y/2, \end{aligned} \tag{2.6}$$

where $d_\ell^x$ and $d_\ell^y$ are the distances between the transmitter and receiver elements in $x$ and $y$ axes, respectively, as shown in Fig. 2.2a. Applying multivariate Taylor series expansion to (2.5) up to third order terms with respect to the parameters $d_\ell^x$ and $d_\ell^y$ around zero, as described in the Appendix C, we can obtain

$$R_\ell \approx 2R + \frac{(d_\ell^x)^2 + (d_\ell^y)^2}{4R} - \frac{((x - x')d_\ell^x + (y - y')d_\ell^y)^2}{4R^3}, \tag{2.7}$$

where

$$R = \sqrt{(x - x')^2 + (y - y')^2 + z_0^2}, \tag{2.8}$$

is the distance between the midpoint and the scatterer. Considering $(x - x'), (y - y') \ll z_0$ for the second order terms in (2.7), we can obtain an improved approximation to the total round-trip distance associated with the $\ell$th virtual element in terms of

$$R_\ell \approx 2R + \frac{(d_\ell^x)^2 + (d_\ell^y)^2}{4z_0}. \tag{2.9}$$

### 2.4 Signal Model

In recent years, several mmWave sensors based on FMCW signaling have been successfully constructed especially targeting automotive radar applications. FMCW (also known as chirp waveform) offers several advantages, i.e., large signal bandwidth, range processing gain, the inherent isolation between transmitters and receivers, and low sampling rate. Based on the improved virtual antenna array concept presented in the previous chapter and TDM technique, the transmit and receive antennas are paired to approximate a monostatic radar operation. Thus, let us briefly review a single element monostatic radar signal model.

Consider an FMCW signal transmitted by the monostatic antenna element in complex form as

$$m(t) = e^{j2\pi(f_0 t + 0.5Kt^2)}, \quad 0 \le t \le T, \tag{2.10}$$

where $f_0$ is the carrier frequency at time $t = 0$, $K = B/T$ is the slope of frequency computed from the sweep bandwidth of $B$, and the chirp duration of $T$. Assuming an ideal point scatter at a distance of $R$, the received signal by the same monostatic antenna element is delayed and scaled version of the transmitted signal

$$\hat{s}(t) = \sigma m(t-\tau) = \sigma e^{j2\pi(f_0(t-\tau)+0.5K(t-\tau)^2)}, \tag{2.11}$$

where $\tau = 2R/c$ is the round-trip delay of the echo for the target distance of $R$, $c$ is the speed of light, and $\sigma$ is the combination of target reflectivity and round-trip amplitude decay with range [25, 30]

$$\sigma = p/R^2, \tag{2.12}$$

where $p$ is the complex reflectivity of the ideal point target. The radar demodulates the received signal by mixing it with a copy of the transmitted signal to reduce the required system sampling rate. This is known as dechirping and results in a complex intermediate frequency (or beat) signal [31]

$$s(t) = \sigma e^{j2\pi(f_0\tau+K\tau t-0.5K\tau^2)}, \tag{2.13}$$

where $K\tau$ term is the beat frequency which carries the range information. The last term of (2.13) is known as the residual video phase (RVP), which is found to be negligible [32]. Therefore, the beat signal can be rewritten in the wavenumber domain as

$$s(k) = p\frac{e^{j2kR}}{R^2}, \quad \frac{2\pi f_0}{c} \leq k \leq \frac{2\pi f_T}{c}, \tag{2.14}$$

where $f_T = f_0 + KT$ is the maximum swap frequency of FMCW radar and $k = 2\pi f/c$ is the wavenumber corresponding to the frequency $f$.

Now we are ready to introduce the midpoint approximation derived in Section 2.3. The approximation in (2.9) allows a MIMO array with sparsely placed transmit and receive elements to be converted to a virtual monostatic array more accurately for near-field imaging applications. The effectiveness of the image reconstruction is mainly determined by proper handling of the phase in (2.14), and any improvement in the amplitude decay with range will

have little impact on the reconstructed image. Therefore, substituting (2.9) into the phase term in (2.14), we can express the received signal by the $\ell$th hypothetical monostatic virtual element as

$$s_\ell(k) \approx p\frac{e^{jkR_\ell}}{R^2} = s(k)e^{j\phi_\ell(k)}, \tag{2.15}$$

where $s(k)$ is the signal that would be received by a physical monostatic element located at the same midpoint between actual transmitter and receiver antennas, and

$$\phi_\ell(k) = k\frac{(d_\ell^x)^2 + (d_\ell^y)^2}{4z_0}, \tag{2.16}$$

is the nonlinear phase term as a result of the improved approximation in (2.9) needed for near-field applications.

In the MIMO-SAR imaging configuration, the acquired 3-D backscattered data cube $s_\ell(x, y, k)$ from the $\ell$th virtual channel is a function of two spatial coordinates, antenna pair spacing, target distance and the wavenumber. If the 2-D distributed target at $z_0$ is characterized by its complex reflectivity function $p(x', y')$, the main purpose of the MIMO-SAR imaging algorithm is to recover $p(x', y')$ from the reflected signals $s_\ell(x, y, k)$ captured by all independent and arbitrary located virtual elements.

# CHAPTER 3

# IMAGE RECONSTRUCTION WITH MONOSTATIC SAR

Here, we review the standard monostatic SAR image reconstruction framework [4, 21], which forms the basis of our proposed algorithms. We adopt the signal model that assumes continuously recorded aperture data. Based on this model, we will determine the important relationship between $k-$domain (or spectral domain) and image domain (or spatial domain) when the imaging aperture is sparsely sampled by MIMO-SAR in Fig. 2.1.

We assume the linearized scattering model with the target reflectivity of $p(x', y')$. By expanding the signal model in (2.14), we can express the received backscattered data from a planar target at a distance of $z_0$ as

$$s(x, y, k) = \iint p(x', y') \frac{e^{j2kR}}{R^2} \, dx' \, dy', \tag{3.1}$$

where $R$ is the distance between the transceiver element and a general point on the target given in (2.8). We include the amplitude factor in the signal model due varying distance of MIMO array to the target. The amplitude factor (i.e., path loss) is typically ignored in the existing derivations. The target points are located at an average distance of $z_0$ from the aperture plane. Therefore, $R^{-2}$ in (3.1) can be approximated by $(z_0 R)^{-1}$. The error introduced by this approximation will be negligible in the near-field applications [33]. $z_0$ is constant for a stationary object and, therefore, it can be ignored. As a result, the 2-D image reconstruction will be effectively approximated by a combination of the phase terms and the retained $R^{-1}$ dependence that yields

$$s(x, y, k) = \iint p(x', y') \frac{e^{j2kR}}{R} \, dx' \, dy'. \tag{3.2}$$

Our derivation builds on the spirit of Weyl's idea [34] of the representation of a spherical wave as a superposition of plane waves [35]

$$\frac{e^{j2kR}}{R} = \frac{j}{2\pi} \iint \frac{e^{j(k_x(x-x')+k_y(y-y')+k_z z_0)}}{k_z}\, dk_x\, dk_y, \tag{3.3}$$

where

$$k_z = \sqrt{4k^2 - k_x^2 - k_y^2}. \tag{3.4}$$

It is important to note that the plane waves are homogeneous when $k_x^2 + k_y^2 \leq 4k^2$, but they are inhomogeneous (significant only close to the plane $z_0 = 0$) otherwise. The entire derivation of (3.3) is given in the Appendix B.

After substituting (3.3) into (3.2), the backscattered data becomes

$$s(x, y, k) = \frac{j}{2\pi} \iiiint p(x', y') \frac{1}{k_z} e^{j(k_x(x-x')+k_y(y-y')+k_z z_0)}\, dk_x\, dk_y\, dx'\, dy'. \tag{3.5}$$

Rearranging the order of integrals and using the 2-D Fourier transform definitions in the Appendix A gives

$$\begin{aligned} s(x, y, k) = \frac{j}{2\pi} \iint \underbrace{\left[ \iint p(x', y') e^{-j(k_x x' + k_y y')}\, dx'\, dy' \right]}_{\mathrm{FT}_{2D}\left[p(x,y)\right] = P(k_x, k_y)} \\ \times \frac{e^{jk_z z_0}}{k_z} e^{j(k_x x + k_y y)}\, dk_x\, dk_y. \end{aligned} \tag{3.6}$$

The distinction between the primed and unprimed coordinate systems above is dropped in the forward Fourier transform operation (denoted as $\mathrm{FT}_{2D}$) because they coincide. The outer double integral above represents a 2-D inverse Fourier transform over the $xy$ domain. Hence, after dropping the constant terms, (3.6) becomes

$$s(x, y, k) = \mathrm{IFT}_{2D}\left[ P(k_x, k_y) \frac{e^{jk_z z_0}}{k_z} \right], \tag{3.7}$$

that yields

$$P(k_x, k_y) = S(k_x, k_y, k) k_z e^{-jk_z z_0}. \tag{3.8}$$

In (3.7), $\text{IFT}_{2D}$ denotes 2-D inverse Fourier transform operation over the $xy$ domain. If the data $s(x, y, k)$ is uniformly sampled in $x$ and $y$, the 2-D fast Fourier transform (FFT) can be used to obtain discrete version of $S(k_x, k_y, k) = \text{FT}_{2D}[s(x, y, k)]$. (3.8) is then evaluated at multiple wavenumbers and coherently summed within an image plane [16] to reconstruct the 2-D target reflectivity as

$$p(x, y) = \int \text{IFT}_{2D}\left[S(k_x, k_y, k) k_z e^{-jk_z z_0}\right] dk. \tag{3.9}$$

Therefore, a monochromatic approach is assumed in the rest of the dissertation proposal and $k$ variable in the backscattered data is dropped for simplicity. The image reconstruction steps are summarized in Algorithm 1. The 2-D forward Fourier transform in the 2nd step acts as a planewave decomposition of the wavefront. The phase and amplitude factors in the 3rd step backpropagate the wavefront from the SAR aperture to the target plane. The 2-D inverse Fourier transform in the 4th step converts from the wavenumber spectrum domain to the spatial domain to construct the final image.

**Algorithm 1** Image reconstruction with monostatic SAR

1: Gather the backscattered data $s(x, y, k)$ for each wavenumber
2: Perform the 2-D forward Fourier transform operation to obtain $S(k_x, k_y, k)$
3: Multiply $S(k_x, k_y, k)$ by $k_z e^{-jk_z z_0}$ using the dispersion relation in (3.4)
4: Perform the 2-D inverse Fourier transform operation to construct the target reflectivity
5: Evaluate the steps from 1 to 4 at multiple wavenumbers and coherently combine the results to form the final image
6: Compute the magnitude and display the data

# CHAPTER 4

# DEVELOPMENT OF IMAGE RECONSTRUCTION WITH SPARSE MIMO-SAR

The mmWave imager prototype presented in this dissertation proposal exploits sparse MIMO array configurations to reduce the cost and scanning time while providing high-resolution imaging. As a first step, we review the analysis of the 1-D spectral domain of the backscattered data in terms of the dimensions of the target and the continuous finite SAR aperture. This analysis will enable us to develop a novel Fourier based imaging formulation compatible with sparsely sampled MIMO-SAR data.

## 4.1 Wavenumber Spectrum Analysis and Sampling Criterion

Consider an imaging scenario, where the target area is centered with respect to the scanning system, as depicted in Fig. 4.1. While the analysis of the wavenumber spectrum here is limited to $x-$axis, the expressions can be easily expanded to $y-$axis. This approach is based on a prior knowledge of the total size of the target region under consideration instead of an unknown physical target geometry.

Denote $\theta_x$ as the limit of the system operating angle in $x-$axis, which is the lesser of the full beamwidth of the antenna or the angle covered by the aperture over the corresponding axis. Assuming the angle subtended by the aperture is less than the beamwidth of the antenna, we can express

$$\sin\theta_x = \frac{(D_x^S + D_x^T)/2}{\sqrt{(D_x^S + D_x^T)^2/4 + z_0^2}}, \tag{4.1}$$

where $D_x^S$ and $D_x^T$ are the SAR and target aperture sizes, respectively, as depicted in Fig. 2.1. As a result, the spectrum of the backscattered signal along $x-$axis will be limited to the region $[-k_x^{\text{bw}}, k_x^{\text{bw}}]$ where $k_x^{\text{bw}}$ is the highest wavenumber component defined as

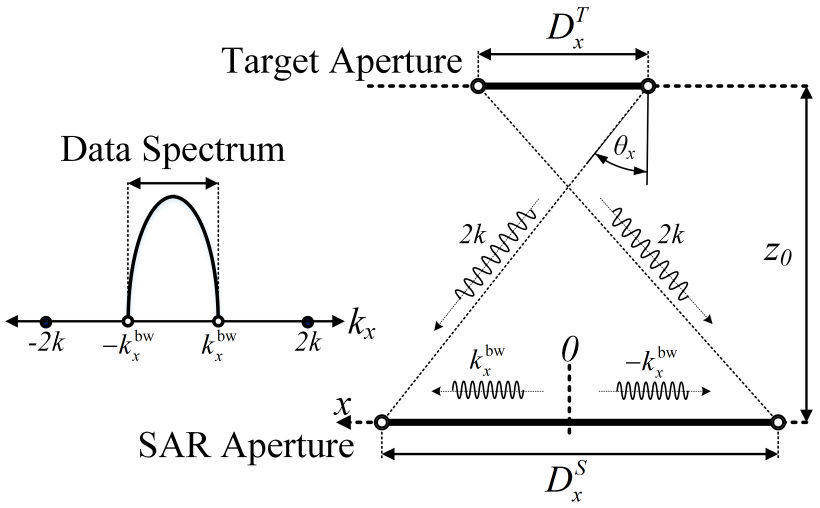


Figure 4.1: Spectral domain of the backscattered data in $x-$axis.

$$k_x^{\mathrm{bw}} \approx 2k \sin\theta_x. \tag{4.2}$$

Substituting (4.1) into (4.2) yields the bandwidth of the backscattered data collected along $x-$axis as

$$k_x^{\mathrm{bw}} \approx \frac{2\pi(D_x^S + D_x^T)}{\lambda\sqrt{(D_x^S + D_x^T)^2/4 + z_0^2}}. \tag{4.3}$$

In MIMO-SAR imaging configuration, the backscattered signals are spatially sampled by transmit/receive antenna locations. While the proposed system employs sparse sampling, its development will be facilitated by understanding of the spatial sampling requirements based on monostatic scenario. As in the traditional time domain signals, sampling needs to satisfy the Nyquist criterion to avoid aliasing, but in space. The maximum theoretical limit of monostatic sampling of infinite aperture is $\lambda/4$ where $\lambda$ is the wavelength [4]. However, the spectrum of the backscattered data captured over a finite SAR aperture is limited by its size, spatial extent of the target aperture, and the distance between both apertures.

Consider a continuous spatial domain signal $s(x)$ captured in an imaging scheme in Fig. 4.1 and its Fourier transform (i.e., its wavenumber spectrum) $S(k_x)$. As expressed in

(4.3), $S(k_x)$ is band-limited to $|k_x| \leq k_x^{\text{bw}}$. The corresponding minimum sampling wavenumber (i.e., the Nyquist rate) along $x-$axis is given by

$$k_x^s \geq 2k_x^{\text{bw}} = \frac{4\pi(D_x^S + D_x^T)}{\lambda\sqrt{(D_x^S + D_x^T)^2/4 + z_0^2}}. \tag{4.4}$$

Hence, $s(x)$ can be perfectly reconstructed from its samples without aliasing as long as the spatial sampling interval is [5]

$$\Delta_x \leq \Delta_x^{\text{Nyq}} = \frac{\pi}{k_x^{\text{bw}}} = \frac{\lambda\sqrt{(D_x^S + D_x^T)^2/4 + z_0^2}}{2(D_x^S + D_x^T)}. \tag{4.5}$$

## 4.2 Image Reconstruction with Sparsely Sampled MIMO-SAR Data

If the spatial sampling intervals $\Delta_x$ and $\Delta_y$ do not meet the Nyquist criterion, aliasing that creates artifacts (i.e., ghosts) in the reconstructed image will occur. In the dissertation, we will propose a method for a sparse MIMO-SAR configuration to perfectly reconstruct alias-free images based on a multichannel combining technique using properly chosen complex gains.

To recover images without any reconstruction artifacts, we will first investigate the response of the sparsely sampled MIMO-SAR imaging system to the target being imaged by establishing properties between spectral and spatial domains. We will derive the analytical response of the reconstructed image to the aliasing components in the subsampled data spectrum. The relation between the wavenumber spectrum of the subsampled backscattered data and the reconstructed image is inherently nonlinear. To our knowledge, there is no prior work on establishing this nonlinear relation. Finally, we will propose a novel algorithm that can be used for MIMO-SAR configurations using arbitrarily distributed transmit and receive antennas.

# CHAPTER 5

# IMAGING HARDWARE PROTOTYPE

## 5.1 System Overview

A mmWave imaging prototype system has been built using commercial off-the-shelf (COTS) components to validate the proposed image reconstruction techniques and theoretical relationships established between image and wavenumber domains. The prototype system consists of a mmWave radar, a two-axis mechanical scanner, a motor controller, and a host personal computer (PC). The mmWave radar is combination of three hardware modules from Texas Instruments: (1) IWR1443-Boost, (2) mmWave-Devpack, and (3) TSW1400 boards as shown in Fig. 5.1a.

IWR1443-Boost is an evaluation module based on the single-chip IWR1443 mmWave sensor. It features FMCW transceiver with a 4 GHz frequency bandwidth from 77 GHz to 81 GHz. It integrates four receive and three transmit antennas making an ideal candidate for sparse MIMO array configurations. Fig 5.2a shows the physical antenna layout of IWR1443-Boost and its corresponding virtual array configuration. In the default layout, the receive antennas are uniformly spaced along $y-$axis by $\lambda/2$ (tuned to the center frequency of 79 GHz). Transmit antennas are also uniformly spaced in $y-$axis by $\lambda$ with the exception of the second transmitter, which has an offset of $\lambda/2$ along $x-$axis. In the imaging experiments, we select different antenna pairs (i.e., virtual channels) to emulate various sparse MIMO operations.

TSW1400 and mmWave-Devpack are add-on boards used with IWR1443-Boost to enable high speed raw data capture for post processing. Captured raw data are imported to the host PC with a serial port for the image reconstruction. All algorithms and software controls are implemented in MATLAB.

The other component of the prototype system is the two-axis mechanical scanner built using linear rails and stepper motors, as shown in Fig. 5.1b. The scanner provides movements

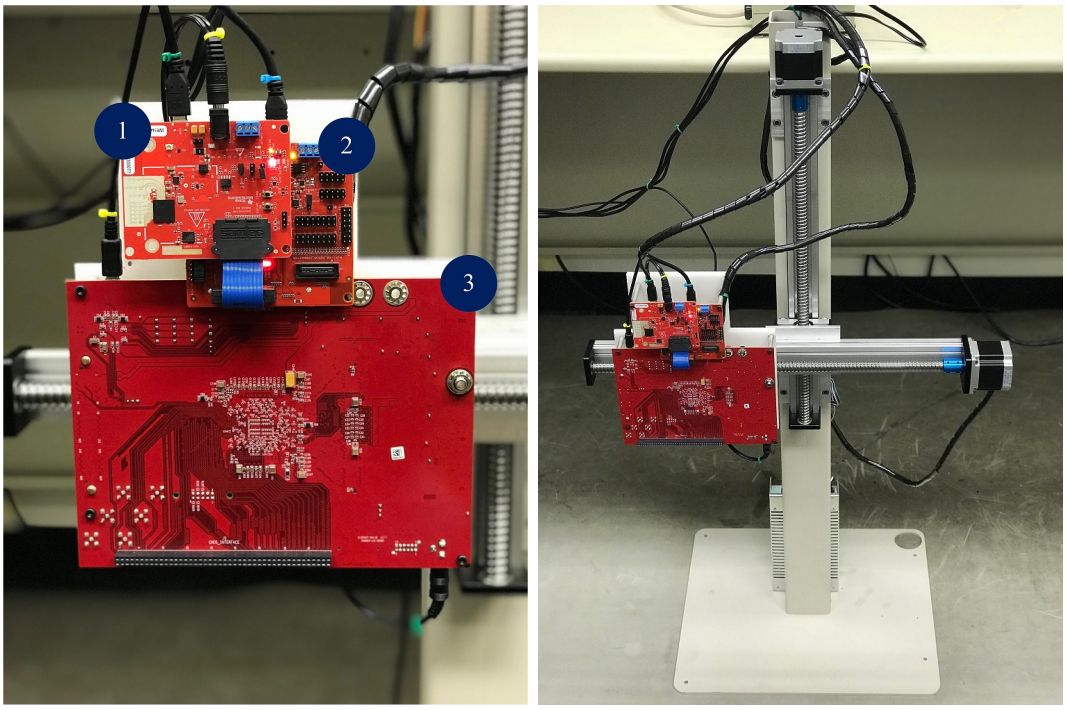


(a) (b)

Figure 5.1: mmWave imager prototype. (a) FMCW radar hardware stack. (b) Two-axis motorized scanner.

in horizontal and vertical directions. The radar hardware stack is installed on the horizontal track by which an equivalent 2-D scanning is achieved. The maximum scanning ranges in both horizontal and vertical directions are 400 mm. The motor controller, which is configured to operate linear rails at a maximum speed of 20 mm/s, is connected to the host PC with a serial port. The positional accuracy of the scanning is about 0.05 mm. While the current scanner is slow, our goal is to demonstrate the proof of concept. We are working on a much faster mechanical scanner, and we will report our results in the dissertation.

The diagram shown in Fig. 5.2b is a simplified view of the main elements and the high-level system architecture of the imaging system. Both radar and rail system are controlled via a MATLAB graphical user interface (GUI) shown in Fig. 5.3.

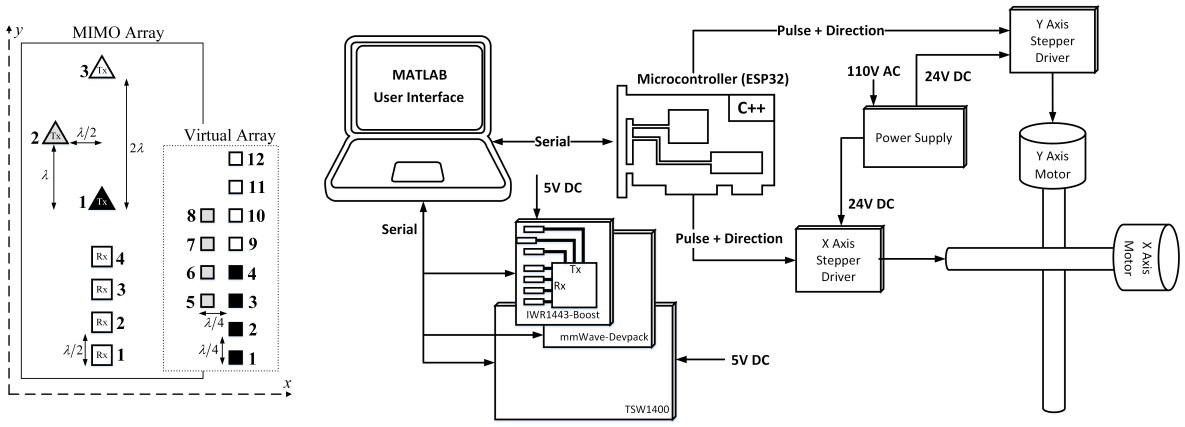


(a) (b)

Figure 5.2: (a) MIMO array topology of IWR1443-Boost with three transmit and four receive antenna elements, and corresponding virtual array. (b) The hardware architecture of mmWave imager prototype.

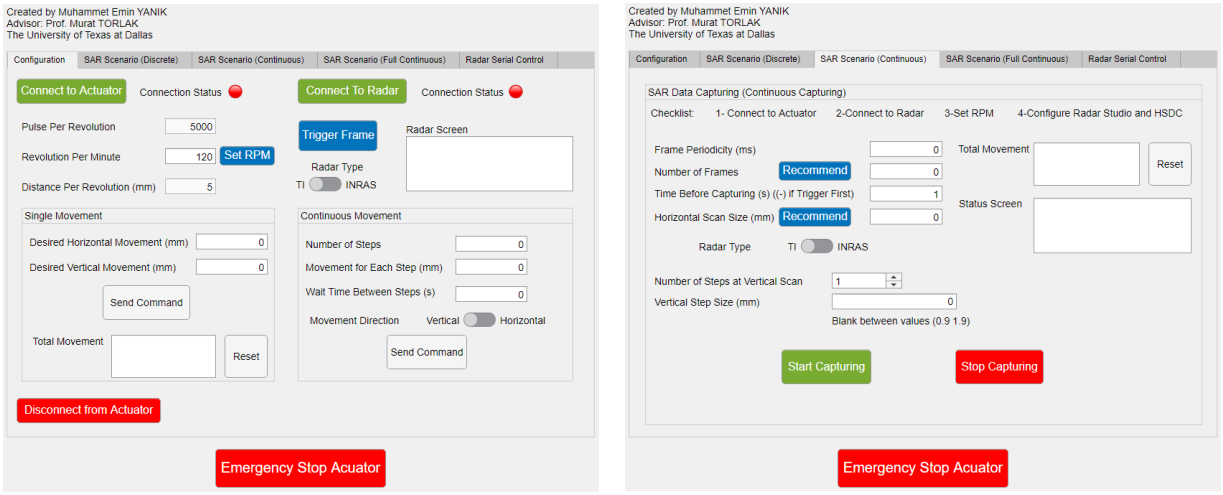


(a) (b)

Figure 5.3: MATLAB GUI for MIMO-SAR imaging. (a) Platform and radar configuration menu tab. (b) SAR scenario generation menu tab.

## 5.2 MIMO Array Calibration

In a practical system, measurement errors in the MIMO array may arise due to sensor gain and phase mismatches [36, 37]. Especially, phase mismatches can affect the image

reconstruction adversely. In fact, the algorithms presented in this dissertation proposal are derived under the assumption that the response of the imaging system is known.

In this dissertation proposal, we utilize a well-known calibration method for multistatic radar systems based on the ideal backscattered signal model from a reference point target (a corner reflector) at a known position. Let us define the total round-trip delay $\tilde{\tau}_\ell$ of the FMCW signal reflected off the point target between the $u$th transmit and $v$th receive antennas, and the corresponding transceiver gain $a_\ell$. We model the delays between antenna pairs as the superposition of a common instrument delay and residual delays between antenna elements: $\tilde{\tau}_\ell = \tau_i + \tau_\ell$. Ignoring the additive noise, the uncalibrated measured beat signal (see Section 2.4) can be defined as

$$\tilde{s}_\ell(t) = a_\ell e^{j2\pi(f_0+Kt)(\tau_i+\tau_\ell)} = \underbrace{\underbrace{a_\ell e^{j\psi_i}}_{\eta_\ell} e^{j2\pi f_i t}}_{w_\ell(t)} s_\ell(t), \tag{5.1}$$

where $s_\ell(t)$ is the reference beat signal model, $f_i = K\tau_i$ is the beat frequency that cause a range bias in the system, and $\eta_\ell$ is the residual complex gain factor. Given the measurements $\tilde{s}_\ell(t)$, the calibration error signal can be computed by a simple demodulation process

$$w_\ell(t) = \tilde{s}_\ell(t) s_\ell^*(t), \tag{5.2}$$

where $(.)^*$ denotes the complex-conjugate operation. Estimating $f_i$ and $\eta_\ell$ from (5.2) reduces to the parameter estimation problem of a single-frequency complex tone from noisy observations [38][39]

$$\hat{f}_i = \arg\max_f \sum_{<\ell>} |W_\ell(f)|^2, \tag{5.3}$$

where $W_\ell(f)$ is defined as

$$W_\ell(f) = \int_0^T w_\ell(t) e^{-j2\pi ft}\, dt. \tag{5.4}$$

Finally, the complex gain factors $\eta_\ell$ for each transceiver pair can be computed by plugging the estimate $\hat{f}_i$ in (5.1).

### 5.3 Image Resolution

The theoretical limit of the spatial resolution achieved in the reconstructed image is determined by width of the coverage in the wavenumber spectrum domain. In one dimension, a spectral coverage of width $\Delta k$ results in a spatial pulsewidth of $2\pi/\Delta k$ [4]. The spatial frequency width of the backscattered data in $k_z-$axis is $2(k_T - k_0)$, where $k_0$ and $k_T$ are the wavenumbers correspond to the lowest and highest operating frequencies of the system ($f_0$ and $f_T$, respectively, in (2.14)). Therefore, the depth ($z-$axis) resolution is determined by the bandwidth as

$$\delta_z \approx \frac{2\pi}{2(k_T - k_0)} = \frac{c}{2(f_T - f_0)} = \frac{c}{2B}. \tag{5.5}$$

Similarly, from Section 4.1, the total bandwidth in the $x$ and $y$ axes are

$$\begin{aligned} \Delta k_x &\approx 2k_x^{\text{bw}} \approx \frac{4\pi(D_x^S + D_x^T)}{\lambda\sqrt{(D_x^S + D_x^T)^2/4 + z_0^2}}, \\ \Delta k_y &\approx 2k_y^{\text{bw}} \approx \frac{4\pi(D_y^S + D_y^T)}{\lambda\sqrt{(D_y^S + D_y^T)^2/4 + z_0^2}}, \end{aligned} \tag{5.6}$$

where the physical lengths of the SAR aperture and the target distance are depicted in Fig. 2.1. Hence, the horizontal ($x-$axis) and vertical ($y-$axis) cross-range resolutions become

$$\delta_x \approx \frac{2\pi}{\Delta k_x} \approx \frac{\lambda\sqrt{(D_x^S + D_x^T)^2/4 + z_0^2}}{2(D_x^S + D_x^T)},$$
$$\delta_y \approx \frac{2\pi}{\Delta k_y} \approx \frac{\lambda\sqrt{(D_y^S + D_y^T)^2/4 + z_0^2}}{2(D_y^S + D_y^T)}. \tag{5.7}$$

For an aperture-limited system with range $z_0$ much greater than the aperture size $D_x^S$ and $D_y^S$, the cross-range resolutions can be approximated for the center of the imaging scene (i.e. $D_x^T = D_y^T = 0$) as [4] [5]

$$\delta_x \approx \frac{\lambda z_0}{2D_x^S}, \quad \delta_y \approx \frac{\lambda z_0}{2D_y^S}. \tag{5.8}$$

# CHAPTER 6

# MEASUREMENTS AND IMAGING RESULTS

The reconstruction quality of the imaging systems is described by the point spread function (PSF). We measure the PSF of our system using a corner reflector. Then, simulations are performed to examine the potential of the proposed algorithms. Finally, the experimental image results of uncovered and concealed targets are provided. In all experiments, FMCW waveforms are configured to vary from $f_0 = 77.38$ GHz to $f_T = 80.93$ GHz, where the signal duration $T \approx 56.02$ $\mu$s and the frequency slope $K \approx 63.37$ MHz/$\mu$s. The wavelength $\lambda$ is computed according to the center frequency of 79 GHz unless otherwise noted. The target distance $z_0$ is estimated from the index of the maximum of the combined range spectrum computed from the beat signals. The image slices obtained at multiple frequencies from $f_0 = 77.38$ GHz to $f_T = 80.93$ GHz are coherently combined to form the final image. Before the image reconstruction process, each subchannel is calibrated as detailed in Section 5.2. All the images presented here are reconstructed on a host PC with Intel Core i7-7700 3.6 GHz central processing unit (CPU) and 64 gigabytes of random access memory (RAM).

## 6.1 Measured Point Spread Function

To demonstrate the experimental image resolution of our hardware prototype, we measure the PSF along $x-$axis between a transmit and receive antenna pair of MIMO radar. The measured PSF is shown in Fig. 6.1. In this measurement, a corner reflector is placed at a distance of $z_0 = 808$ mm in front of the scanner. The scanner moves the radar along $x-$axis. The speed of the scan and radar chirp intervals are configured such that a sampling distance of $\Delta_x \approx 0.96$ mm ($\approx \lambda/4$) is realized. The SAR aperture length is $D_x^S = 400$ mm along the scanning direction. As given in (5.7), the theoretical image resolution under this configuration is about $\delta_x \approx 4$ mm. As shown in Fig. 6.1, the measured PSF demonstrates the same theoretical image resolution.

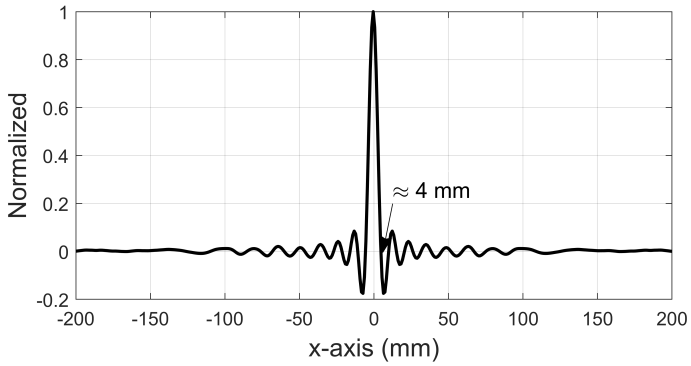


Figure 6.1: Measured PSF along $x-$axis provides the lateral image resolution that can be achieved by the imaging prototype system at a distance of 808 mm.

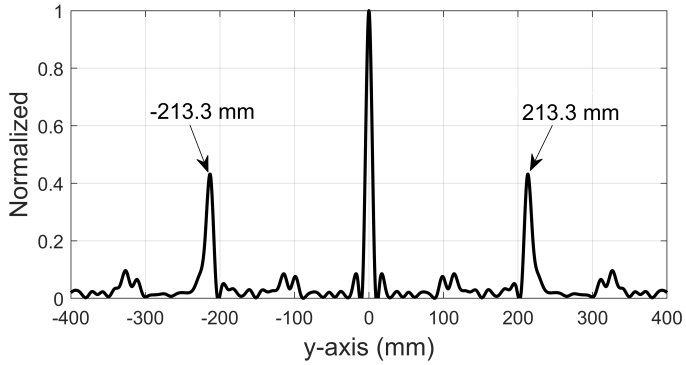


Figure 6.2: Measured PSF along $y-$axis demonstrates the impact of subsampling in spatial domain. Two visible artifacts are due to aliasing within the visible region.

An important contribution of this investigation is to establish the analytical relationship between imaging ambiguities and the subsampled SAR aperture parameters. The measured response of a single transceiver pair along $y-$axis generated with a sampling distance of $\Delta_y = 7.59$ mm (well over the required Nyquist interval) shows the presence of two imaging artifacts (i.e., ghosts), as shown in Fig. 6.2. In this experiment, the same corner reflector is placed at a distance of $z_0 = 808$ mm in front of the imager. The radar is configured with the same chirp parameters. In the dissertation, we will verify the positions of two artifacts along the $y-$axis due to subsampling analytically.

## 6.2 Simulated Imaging Results

To evaluate the performance of the proposed algorithm for recovering ghost-free images when both axes are subsampled, a simulation scenario is performed. A 50 mm by 75 mm small test target, which has different types of small cutouts, is simulated and placed at a distance of $z_0 = 282$ mm from the scanner. The size of the SAR aperture is $D_x^S \approx 200$ mm by $D_y^S \approx 200$ mm. The spatial sampling intervals are selected as $\Delta_x = \Delta_y = 8$ mm. An arbitrary sparse MIMO array with three transmit and three receive antennas shown in Fig.6.3a and Fig.6.3b is simulated.

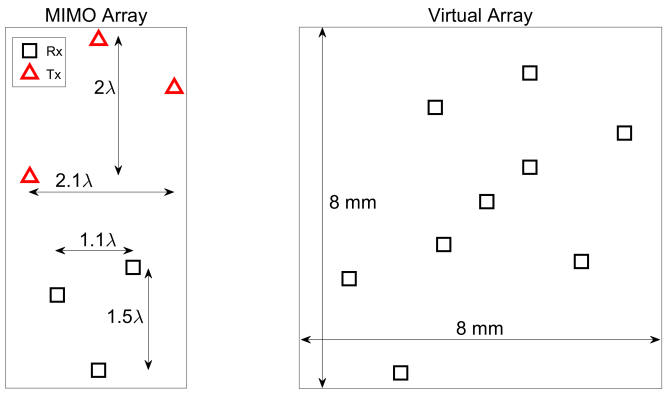


(a) (b)

Figure 6.3: (a) Simulated sparse MIMO array with three transmit and three receive antenna elements, and (b) corresponding virtual array.

SAR aperture is subsampled along both $x$ and $y$ axes. The reconstructed image shown in Fig. 6.4a using a single virtual channel shows eight ghosts targets within the visible region of 200 mm $\times$ 200 mm as expected. Fig. 6.4b shows the alias-free image obtained using nine sparse channels with properly chosen complex gains such that the all eight ghosts are canceled. On the other hand, an ideal imaging system, which needs $\lambda/4 \approx 0.95$ mm spacing between the measurement points, would employ a uniform 2-D array with about 80 virtual elements. In the dissertation, proposed image reconstruction algorithms with subsampled SAR aperture will be validated experimentally with real measurements.

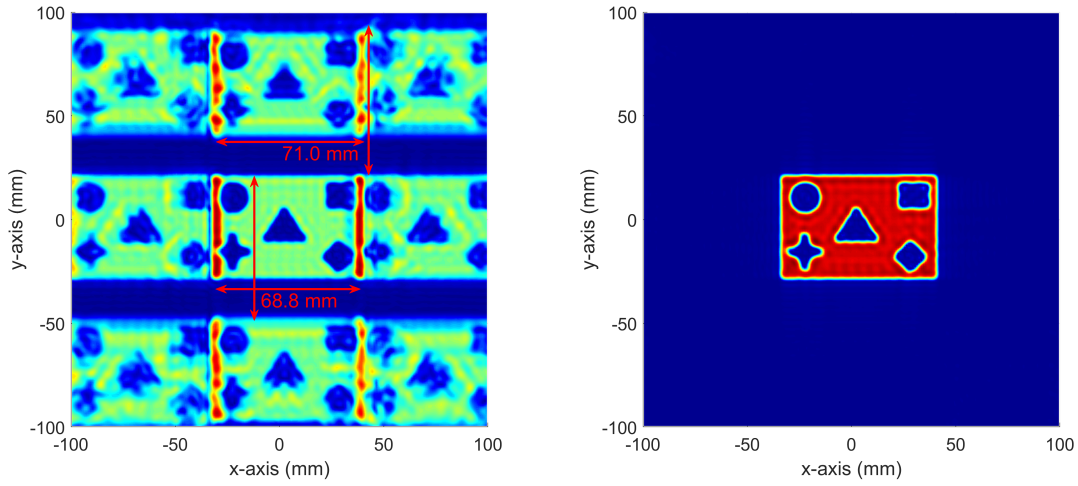


(a) (b)

Figure 6.4: Simulated image reconstruction scenario with sparsely sampled aperture data: (a) reconstructed image from single channel (1st), and (b) reconstructed image from nine channels combined using properly chosen $w$ gains.

### 6.3 Experimental Imaging Results

The imaging process and the prototyped system presented in this dissertation proposal are experimentally verified with screening various targets. Table 6.1 summarizes the common system parameters used in each experiment.

Table 6.1: Summary of the system parameters for each experiment

| Parameter | Fig. 6.5 | Fig. 6.7 | Fig. 6.8 | Fig. 6.9 |
|---|---|---|---|---|
| $B$ (GHz) | 3.55 | 3.55 | 3.55 | 3.55 |
| $K$ (MHz/$\mu$s) | 63.37 | 63.37 | 63.37 | 63.37 |
| $T$ ($\mu$s) | 56.02 | 56.02 | 56.02 | 56.02 |
| $D_x$ (mm) | 300 | 200 | 400 | 400 |
| $D_y$ (mm) | 300 | 200 | 400 | 400 |
| $z_0$ (mm) | 300 | 300 | 270 | 254 |
| $\Delta_x$ (mm) | 0.95 | 0.5 | 0.98 | 0.98 |
| $\Delta_y$ (mm) | 3.795 | 2 | 7.59 | 7.59 |

In the first imaging experiment, small wrenches shown in Fig. 6.5a and Fig. 6.5c are selected to serve as targets to illustrate the effectiveness of the system using a uniform virtual

array. For both scenarios, the target distance is $z_0 = 300$ mm and the SAR aperture size is about 300 mm $\times$ 300 mm. Under this configuration, the lateral resolution is approximately 2 mm. The spatial sampling intervals are selected as $\Delta_x \approx 0.95$ mm and $\Delta_y = 3.795$ mm. The reconstructed images are presented in Fig. 6.5b and 6.5d. It is clearly observed that the wrenches are well resolved in the imaging results.

The second imaging experiment demonstrates the capability of the prototyped system for screening of concealed items by using a single transceiver moving along the 2-D aperture. A small test target with a size of 50 mm by 75 mm is cut out from a copper clad laminate to create a similar imaging setup to simulations. The test target has similar small cutouts as shown in Fig. 6.6a. For each experiment, the target is placed at a $z_0 = 300$ mm distance from the radar. The SAR aperture is synthesized to cover an area of $D_x^S \approx 200$ mm by $D_y^S \approx 200$ mm. Under this configuration, the resolution in both directions is about 3 mm. The spatial sampling steps are about $\Delta_x \approx 0.5$ mm and $\Delta_y = 2$ mm mm along the horizontal and vertical axes, respectively. They both satisfy the Nyquist sampling criteria in (4.5).

First, the target is concealed in a paper envelope as shown in Fig. 6.6b. The reconstructed image of this scenario is presented in Fig. 6.7b. Then, the same target is concealed in a bag as shown in Fig. 6.6c. The reconstructed image of this scenario is presented in Fig. 6.7c. Finally, the same target is concealed in a cardboard box as shown in Fig. 6.6d. The reconstructed image of this scenario is presented in Fig. 6.7d. The patch with the small cutouts can be identified clearly in all images.

Finally, two additional experiments are performed to demonstrate the capability of the prototyped system in real-world security screening scenarios. In both experiments, the SAR aperture size is about 400 mm $\times$ 400 mm. The spatial sampling intervals are selected as $\Delta_x \approx 0.98$ mm and $\Delta_y = 7.59$ mm. For both scenarios, the lateral resolution achieved is about 1.6 mm.

The imaging scenario in Fig. 6.8a shows multiple objects (two different wire cutters, a pair of scissors, a wire stripper, and a pair of tweezers) concealed in a cardboard box. Fig.

(a)

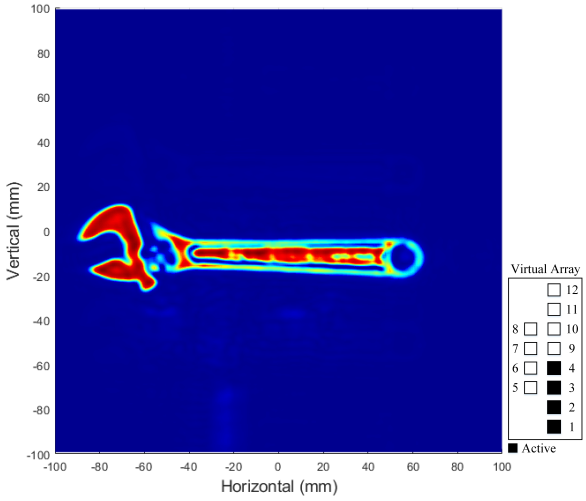


(b)

(c)

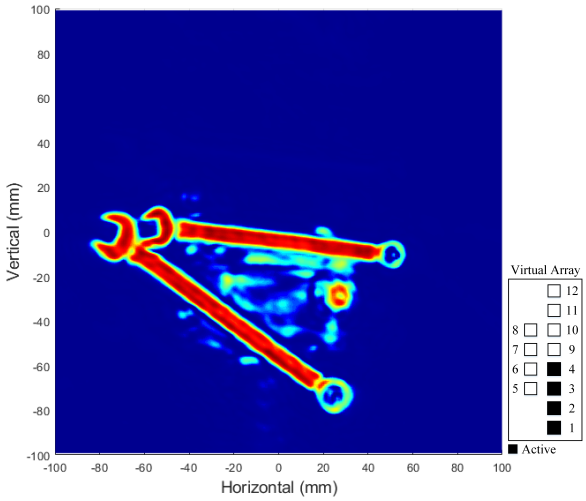


(d)

Figure 6.5: Various experimental images of small wrenches: (a) optical image of a single wrench, (b) reconstructed image from four channels, (c) optical image of two wrenches, (d) reconstructed image from four channels.

6.8b shows the reconstructed image focused at $z_0 = 270$ mm. All the objects are clearly visible without spatial aliasing.

Fig. 6.9a shows the final imaging scenario for a security screening application. Smaller objects (a pair of small scissors, two coins, a knife, a nail clipper, a pair of small tweezers, a


(a) (b)

(c) (d)

Figure 6.6: Concealment scenarios of the target with various cutouts: (a) uncovered, (b) concealed in an envelope, (c) concealed in a bag, and (d) concealed in a cardboard box.

key, and a leather wallet) are concealed in a leather bag. Fig. 6.9b shows the reconstructed image focused at $z_0 = 254$ mm. All the objects are clearly identified, even the non-metallic wallet and very small objects such as key and nail cutter.

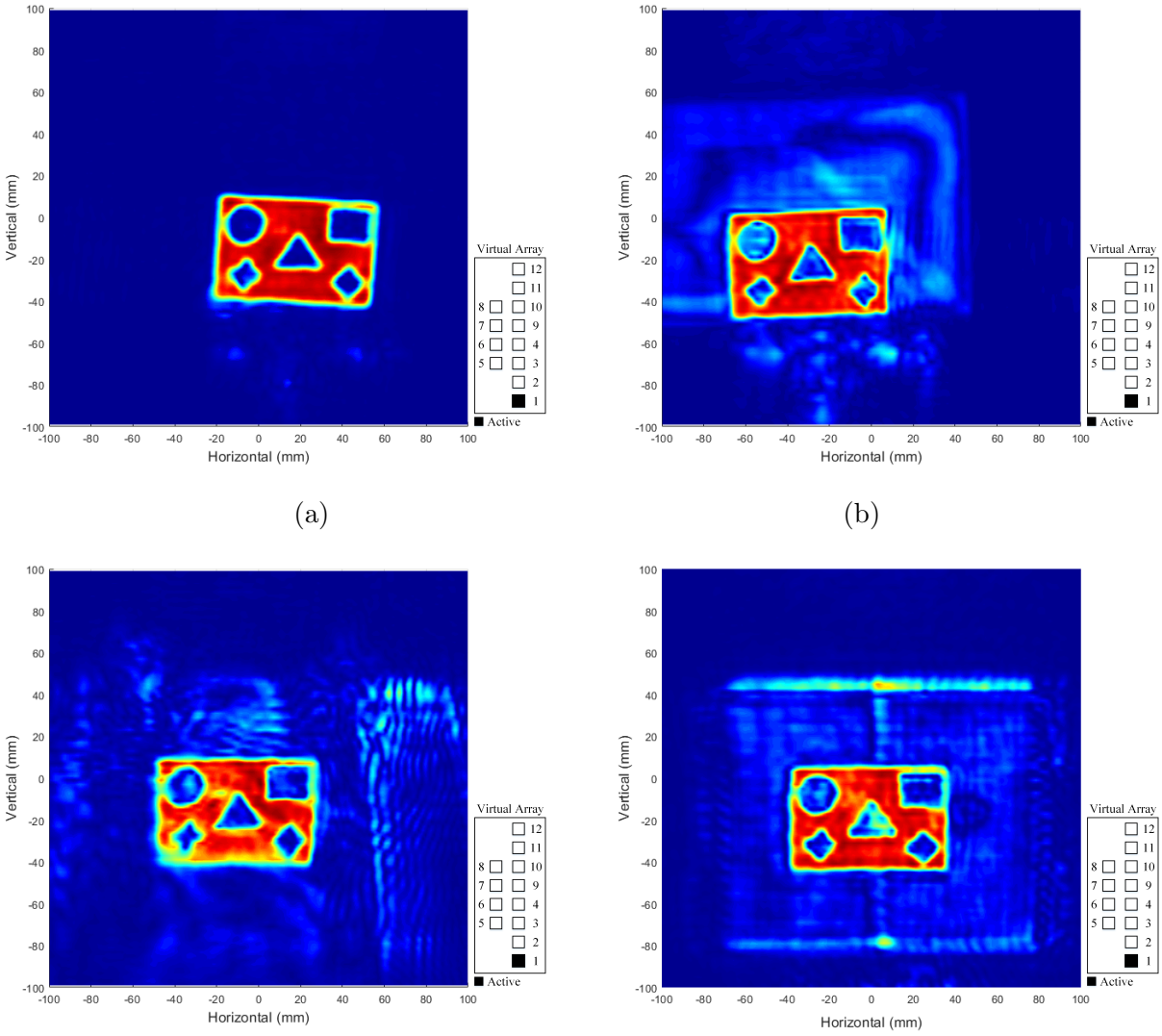


Figure 6.7: Reconstructed images of the target with various cutouts: (a) uncovered, (b) concealed in an envelope, (c) concealed in a bag, and (d) concealed in a cardboard box.

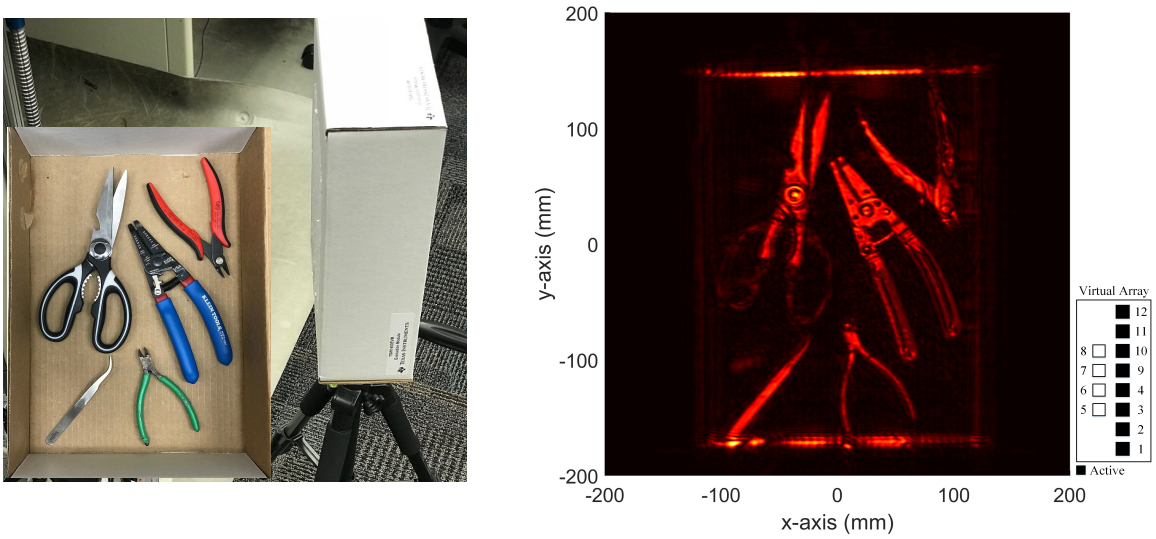


(a) (b)

Figure 6.8: Imaging scenario with multiple objects concealed in a cardboard box: (a) optical image, and (b) reconstructed image from eight channels.

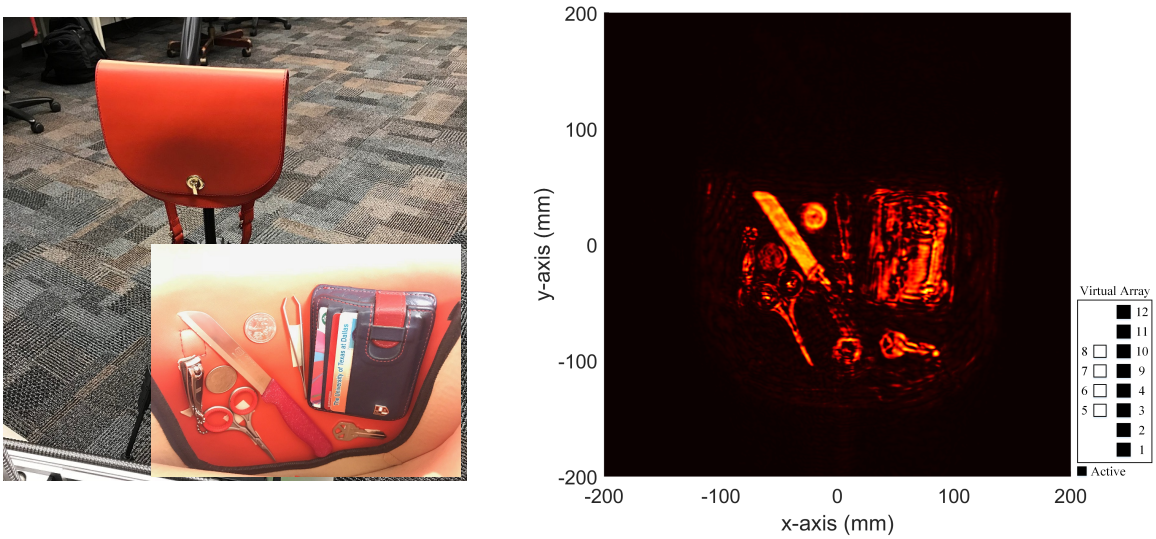


(a) (b)

Figure 6.9: Imaging scenario with small items concealed in a leather bag: (a) optical image, and (b) reconstructed image from eight channels.

# CHAPTER 7

# SUMMARY AND PROPOSED WORK

## 7.1 Summary

In this dissertation proposal, we presented a near-field mmWave imaging system utilizing 2-D MIMO array in SAR configuration. We proposed and experimentally verified a computationally efficient novel image reconstruction algorithm based on sparsely sampled aperture data. We analyzed the effect of sparse sampling both on wavenumber spectrum and spatial domains. We involved the calibration method for MIMO array, as well as the complete signal processing chain necessary for the image formation. We investigated the design considerations including the system's bandwidth, spatial sampling criteria, and image resolution. We built a mmWave imaging prototype using commercially available MIMO sensors to validate the proposed image reconstruction method with measurements. We characterized the system performance by the evaluation of PSF, simulations, and real images. The results show that the prototyped system is able to achieve high image quality with a significantly reduced number of antenna elements, thus making the system more affordable and less complex.

## 7.2 Proposed Work

In this dissertation proposal, the target is assumed to be a 2-D object and parallel to the scanning plane. However, real-world applications should exploit the 3-D holographic imaging capability. Hence, we are developing a complete signal processing chain for a novel low-complexity 3-D image reconstruction approach. We will report our results in the dissertation.

We designed a system-level imager prototype with limited speed and aperture size to demonstrate the proof of concept. Currently, we are improving the imaging system with a much faster and bigger mechanical scanner to work towards real-time applications. Besides,

we will integrate multi-chip cascaded mmWave sensors to create larger MIMO apertures to reduce the total scanning time. We will report our results in the dissertation.

# APPENDIX A

# FOURIER TRANSFORM DEFINITIONS

The 2-D spatial Fourier transform and its inverse are defined by

$$\begin{aligned} S(k_x, k_y) &= \iint s(x,y) e^{-j(k_x x + k_y y)}\, dx\, dy \\ &= \mathrm{FT}_{2D}\big[s(x,y)\big], \end{aligned} \tag{A.1}$$

$$\begin{aligned} s(x,y) &= \frac{1}{(2\pi)^2} \iint S(k_x, k_y) e^{j(k_x x + k_y y)}\, dk_x\, dk_y \\ &= \mathrm{IFT}_{2D}\big[S(k_x, k_y)\big]. \end{aligned} \tag{A.2}$$

If the function is shifted in the spatial domain, there is a corresponding phase shift in the Fourier domain:

$$\mathrm{FT}_{2D}\big[s(x - x_0, y - y_0)\big] = e^{-j(k_x x_0 + k_y y_0)} S(k_x, k_y). \tag{A.3}$$

If the function is shifted in the Fourier domain, there is a corresponding phase shift in the spatial domain:

$$\mathrm{IFT}_{2D}\big[S(k_x - k_0^x, k_y - k_0^y)\big] = e^{j(k_0^x x + k_0^y y)} s(x,y). \tag{A.4}$$

The 2-D spatial Fourier transform of a 2-D spatial impulse train is given by

$$\begin{aligned} &\mathrm{FT}_{2D}\left[\sum_{p\in\mathbb{Z}}\sum_{q\in\mathbb{Z}} \delta(x - p\Delta_x, y - q\Delta_y)\right] \\ &\quad = \frac{(2\pi)^2}{\Delta_x \Delta_y} \sum_{m\in\mathbb{Z}}\sum_{n\in\mathbb{Z}} \delta(k_x - m k_x^s, k_y - n k_y^s), \end{aligned} \tag{A.5}$$

where $k_x^s$ and $k_y^s$ are the spatial sampling frequencies.

Multiplication in the spatial domain corresponds to a convolution in the Fourier domain:

$$\mathrm{FT}_{2D}\big[s_1(x,y) s_2(x,y)\big] = \frac{1}{(2\pi)^2} S_1(k_x, k_y) \circledast S_2(k_x, k_y). \tag{A.6}$$

Differentiation in the spatial domain yields

$$\begin{aligned} \mathrm{FT}_{2D}\left[\frac{\partial s(x,y)}{\partial x}\right] &= jk_x S(k_x,k_y), \\ \mathrm{FT}_{2D}\left[\frac{\partial s(x,y)}{\partial y}\right] &= jk_y S(k_x,k_y). \end{aligned} \tag{A.7}$$

# APPENDIX B

# THE METHOD OF STATIONARY PHASE

The method of stationary phase (MSP) provides an analytical solution for integrands, which have a wide phase variation and an envelope of $g(x, y)$, as [40] [41]

$$\iint g(x,y)e^{j\phi(x,y)}\,dx\,dy \approx \frac{j2\pi}{\sqrt{\phi_{xx}\phi_{yy}-\phi_{xy}^2}} \times g(x_0,y_0)e^{j\phi(x_0,y_0)}, \tag{B.1}$$

where $\phi(x, y)$ is the phase of the exponential that is assumed to be twice-continuously differentiable. A small neighborhood near the points, where the two first derivatives of $\phi(x, y)$ vanish, gives the major contribution to the integral in (B.1). These points are known as points of stationary phase, where the phase $\phi(x, y)$ takes an extreme value as

$$\begin{aligned} \left.\frac{\partial\phi(x,y)}{\partial x}\right|_{(x=x_0,y=y_0)} &= 0, \\ \left.\frac{\partial\phi(x,y)}{\partial y}\right|_{(x=x_0,y=y_0)} &= 0. \end{aligned} \tag{B.2}$$

In (B.1), $\phi_{xx}$, $\phi_{yy}$, and $\phi_{xy}$ denote the second partial derivatives of $\phi(x, y)$ evaluated at the stationary points. It is assumed that $\phi_{xx}\phi_{yy} - \phi_{xy}^2 \neq 0$. The derivation of (B.1) is already given in previous studies for single variable [42] or without an envelope $g(x, y)$ factor [21]. Here, the exact analytical solution is given to evaluate the 2-D Fourier transform of spherical wave formula in (3.3) asymptotically by using MSP.

Substituting (2.8) into (3.3), the spherical wave formula becomes

$$\frac{e^{j2kR}}{R} = \frac{e^{j2k\sqrt{(x-x')^2+(y-y')^2+z_0^2}}}{\sqrt{(x-x')^2+(y-y')^2+z_0^2}}. \tag{B.3}$$

Using the Fourier transform definitions in Appendix A, the 2-D Fourier transform of (B.3) is evaluated as

$$\mathrm{FT}_{2D}\left[\frac{e^{j2kR}}{R}\right] = e^{-j(k_x x' + k_y y')} \times \iint \frac{e^{j2k\sqrt{x^2+y^2+z_0^2}}}{\sqrt{x^2+y^2+z_0^2}} e^{-j(k_x x + k_y y)}\, dx\, dy. \tag{B.4}$$

The double integral above can be solved analytically using MSP in (B.1). Let us define the phase and the envelope terms in (B.4) as

$$\phi(x,y) = 2k\sqrt{x^2+y^2+z_0^2} - k_x x - k_y y, \tag{B.5}$$

$$g(x,y) = 1/\sqrt{x^2+y^2+z_0^2}. \tag{B.6}$$

The first derivatives of (B.5)

$$\begin{aligned} \phi_x(x,y) &= \frac{\partial \phi(x,y)}{\partial x} = \frac{2kx}{\sqrt{x^2+y^2+z_0^2}} - k_x, \\ \phi_y(x,y) &= \frac{\partial \phi(x,y)}{\partial y} = \frac{2ky}{\sqrt{x^2+y^2+z_0^2}} - k_y, \end{aligned} \tag{B.7}$$

give the stationary points in (B.2) as

$$\begin{aligned} x_0 &= \frac{k_x z_0}{\sqrt{4k^2 - k_x^2 - k_y^2}}, \\ y_0 &= \frac{k_y z_0}{\sqrt{4k^2 - k_x^2 - k_y^2}}. \end{aligned} \tag{B.8}$$

In order to ensure the asymptotic expansion provided by the MSP valid, the coordinates must be both real such that the frequency wavenumber must satisfy the following inequality

$$k_x^2 + k_y^2 \leq 4k^2. \tag{B.9}$$

Substituting (B.8) into (B.5) and (B.6), the phase and the envelope evaluated at the stationary points yield

$$\phi(x_0, y_0) = \sqrt{4k^2 - k_x^2 - k_y^2}\, z_0, \tag{B.10}$$

$$g(x_0, y_0) = \frac{\sqrt{4k^2 - k_x^2 - k_y^2}}{2kz_0}, \tag{B.11}$$

respectively. Similarly, the second partial derivatives of the phase evaluated at the stationary points are calculated as

$$\begin{aligned} \phi_{xx} &= \frac{\sqrt{4k^2 - k_x^2 - k_y^2}(4k^2 - k_x^2)}{4k^2 z_0}, \\ \phi_{yy} &= \frac{\sqrt{4k^2 - k_x^2 - k_y^2}(4k^2 - k_y^2)}{4k^2 z_0}, \\ \phi_{xy} &= -\frac{\sqrt{4k^2 - k_x^2 - k_y^2} k_x k_y}{4k^2 z_0}, \end{aligned} \tag{B.12}$$

which yields the denominator in (B.1) as

$$\sqrt{\phi_{xx}\phi_{yy} - \phi_{xy}^2} = \frac{(4k^2 - k_x^2 - k_y^2)}{2kz_0}. \tag{B.13}$$

Substituting (B.10), (B.11) and (B.13) into (B.1), the resulting 2-D Fourier transform expression in (B.4) is expressed as

$$\mathrm{FT}_{2D}\left[\frac{e^{j2kR}}{R}\right] = \frac{j2\pi}{k_z} e^{-j(k_x x' + k_y y' - k_z z_0)}, \tag{B.14}$$

where the spatial wavenumber $k_z$ is given in (3.4). Finally, from the 2-D inverse Fourier transform operation in Appendix A, the spherical wave formula is computed as

$$\frac{e^{j2kR}}{R} = \frac{j}{2\pi} \iint \frac{e^{j(k_x(x-x') + k_y(y-y') + k_z z_0)}}{k_z}\, dk_x\, dk_y. \tag{B.15}$$

# APPENDIX C

# MULTIVARIATE TAYLOR SERIES EXPANSION

Let $f$ be an infinitely differentiable real or complex-valued function in some open neighborhood around $(x, y) = (x_0, y_0)$. Let $\mathbf{x} = \begin{bmatrix} x & y \end{bmatrix}$ and let $\mathbf{x_0} = \begin{bmatrix} x_0 & y_0 \end{bmatrix}$. With this vector notation, the Taylor series of $f(\mathbf{x})$ in a neighborhood of $\mathbf{x_0}$ is

$$\begin{aligned} f(\mathbf{x}) =& f(\mathbf{x_0}) + [(\mathbf{x} - \mathbf{x_0}) \cdot \nabla \mathbf{f}(\mathbf{x_0})] \\ &+ \frac{1}{2!}[(\mathbf{x} - \mathbf{x_0}) \cdot \mathbf{H}(\mathbf{x_0}) \cdot (\mathbf{x} - \mathbf{x_0})^T] + \ldots, \end{aligned} \tag{C.1}$$

where $\nabla \mathbf{f}$ is the vector of first derivatives

$$\nabla \mathbf{f}(x, y) = \begin{bmatrix} f_x(x, y) \\ f_y(x, y) \end{bmatrix}, \tag{C.2}$$

and $\mathbf{H}$ is the matrix of second derivatives, called the Hessian matrix

$$\mathbf{H}(x, y) = \begin{bmatrix} f_{xx}(x, y) & f_{xy}(x, y) \\ f_{yx}(x, y) & f_{yy}(x, y) \end{bmatrix}. \tag{C.3}$$

## C.1 Taylor Series Expansion of the Round-Trip Distance

Substituting the transmitter and receiver locations in (2.6) into (2.5), the total round-trip distance associated with the $u$th transmitter element at $(x_u, y_u, 0)$ and the $v$th receiver element at $(x_v, y_v, 0)$ to a point scatterer at $(x', y', z_0)$ becomes

$$\begin{aligned} R_\ell = & \sqrt{(x + d_\ell^x/2 - x')^2 + (y + d_\ell^y/2 - y')^2 + z_0^2} \\ &+ \sqrt{(x - d_\ell^x/2 - x')^2 + (y - d_\ell^y/2 - y')^2 + z_0^2}. \end{aligned} \tag{C.4}$$

Evaluating the first derivatives of (C.4) at $(d_\ell^x = 0, d_\ell^y = 0)$ yields

$$\left.\frac{\partial R_\ell}{\partial d_\ell^x}\right|_{(d_\ell^x=0,d_\ell^y=0)} = \left.\frac{\partial R_\ell}{\partial d_\ell^y}\right|_{(d_\ell^x=0,d_\ell^y=0)} = 0. \tag{C.5}$$

Similarly, the second partial derivatives of (C.4) evaluated at $(d_\ell^x = 0, d_\ell^y = 0)$ yields

$$\begin{aligned}
\left.\frac{\partial^2 R_\ell}{\partial (d_\ell^x)^2}\right|_{(d_\ell^x=0,d_\ell^y=0)} &= \frac{1}{2R}\left[1 - \frac{(x-x')^2}{R^2}\right], \\
\left.\frac{\partial^2 R_\ell}{\partial (d_\ell^y)^2}\right|_{(d_\ell^x=0,d_\ell^y=0)} &= \frac{1}{2R}\left[1 - \frac{(y-y')^2}{R^2}\right], \\
\left.\frac{\partial^2 R_\ell}{\partial d_\ell^x \partial d_\ell^y}\right|_{(d_\ell^x=0,d_\ell^y=0)} &= -\frac{(x-x')(y-y')}{2R^3},
\end{aligned} \tag{C.6}$$

where $R$ is given in (2.8). Substituting (C.5) and (C.6) into (C.1), quadratic approximation of $R_\ell$ is given by

$$R_\ell \approx 2R + \frac{(d_\ell^x)^2 + (d_\ell^y)^2}{4R} - \frac{((x-x')d_\ell^x + (y-y')d_\ell^y)^2}{4R^3}. \tag{C.7}$$

## REFERENCES


[1] L. Chao, M. N. Afsar, and K. A. Korolev, "Millimeter wave dielectric spectroscopy and breast cancer imaging," in *IEEE 7th European Microwave Integrated Circuit Conf.*, Amsterdam, Netherlands, Oct. 2012, pp. 572–575.

[2] S. D. Meo, G. Matrone, M. Pasian, M. Bozzi, L. Perregrini, G. Magenes, A. Mazzanti, F. Svelto, P. E. Summers, G. Renne, L. Preda, and M. Bellomi, "High-resolution mm-wave imaging techniques and systems for breast cancer detection," in *IEEE MTT-S Int. Microwave Workshop Series on Advanced Materials and Processes for RF and THz Applications*, Pavia, Italy, Sep. 2017, pp. 1–3.

[3] Y. Gao and R. Zoughi, "Millimeter wave reflectometry and imaging for noninvasive diagnosis of skin burn injuries," *IEEE Trans. on Instrumentation and Measurement*, vol. 66, no. 1, pp. 77–84, Jan. 2017.

[4] D. M. Sheen, D. L. McMakin, and T. E. Hall, "Three-dimensional millimeter-wave imaging for concealed weapon detection," *IEEE Trans. on Microwave Theory and Techniques*, vol. 49, no. 9, pp. 1581–1592, Sep. 2001.

[5] X. Zhuge and A. G. Yarovoy, "A sparse aperture MIMO-SAR-based UWB imaging system for concealed weapon detection," *IEEE Trans. on Geoscience and Remote Sensing*, vol. 49, no. 1, pp. 509–518, Jan. 2011.

[6] S. S. Ahmed, A. Schiessl, F. Gumbmann, M. Tiebout, S. Methfessel, and L. Schmidt, "Advanced microwave imaging," *IEEE Microwave Magazine*, vol. 13, no. 6, pp. 26–43, Sep. 2012.

[7] R. Appleby and R. N. Anderton, "Millimeter-wave and submillimeter-wave imaging for security and surveillance," *Proc. of the IEEE*, vol. 95, no. 8, pp. 1683–1690, Aug. 2007.

[8] J. L. Fernandes, J. R. Tedeschi, D. M. Sheen, and D. L. McMakin, "Three-dimensional millimeter-wave imaging for concealed threat detection in shoes," in *Proc. SPIE, Passive and Active Millimeter-Wave Imaging XVI*, vol. 8715, Baltimore, MD, USA, May 2013, pp. C1–C8.

[9] M. E. Yanik and M. Torlak, "Near-field 2-D SAR imaging by millimeter-wave radar for concealed item detection," in *Proc. IEEE Radio and Wireless Symposium*, Orlando, FL, USA, Jan. 2019.

[10] S. Kharkovsky, J. T. Case, M. A. Abou-Khousa, R. Zoughi, and F. L. Hepburn, "Millimeter-wave detection of localized anomalies in the space shuttle external fuel tank insulating foam," *IEEE Trans. on Instrumentation and Measurement*, vol. 55, no. 4, pp. 1250–1257, Aug. 2006.

[11] K. Ramasubramanian and J. Singh, "AWR1443 single-chip radar: for diverse proximity-sensing applications," Texas Instruments, Tech. Rep. SPYY008, May 2017.

[12] D. W. Bliss and K. W. Forsythe, "Multiple-input multiple-output (MIMO) radar and imaging: degrees of freedom and resolution," in *The 37th Asilomar Conf. on Signals, Systems and Computers*, vol. 1, Pacific Grove, CA, USA, Nov. 2003, pp. 54–59.

[13] J. Li and P. Stoica, *MIMO Radar Signal Processing*, ser. John Wiley & Sons, 2009.

[14] ——, "MIMO radar with colocated antennas," *IEEE Signal Processing Magazine*, vol. 24, no. 5, pp. 106–114, Sep. 2007.

[15] S. S. Ahmed, A. Schiessl, and L. Schmidt, "A novel fully electronic active real-time imager based on a planar multistatic sparse array," *IEEE Trans. on Microwave Theory and Techniques*, vol. 59, no. 12, pp. 3567–3576, Dec. 2011.

[16] W. F. Moulder, J. D. Krieger, J. J. Majewski, C. M. Coldwell, H. T. Nguyen, D. T. Maurais-Galejs, T. L. Anderson, P. Dufilie, and J. S. Herd, "Development of a high-throughput microwave imaging system for concealed weapons detection," in *IEEE International Symposium on Phased Array Systems and Technology*, Waltham, MA, USA, Oct. 2016, pp. 1–6.

[17] M. A. Richards, "A beginner's guide to interferometric SAR concepts and signal processing [AESS tutorial IV]," *IEEE Aerospace and Electronic Systems Magazine*, vol. 22, no. 9, pp. 5–29, Sep. 2007.

[18] G. Franceschetti and R. Lanari, *Synthetic Aperture Radar Processing*, ser. New York: CRC Press, 1999.

[19] R. Zhu, J. Zhou, G. Jiang, and Q. Fu, "Range migration algorithm for near-field MIMO-SAR imaging," *IEEE Geoscience and Remote Sensing Letters*, vol. 14, no. 12, pp. 2280–2284, Dec. 2017.

[20] M. Soumekh, "Wide-bandwidth continuous-wave monostatic/bistatic synthetic aperture radar imaging," in *Proc. Int. Conf. on Image Processing*, vol. 3, Chicago, IL, USA, Oct. 1998, pp. 361–365.

[21] J. M. Lopez-Sanchez and J. Fortuny-Guasch, "3-D radar imaging using range migration techniques," *IEEE Trans. on Antennas and Propagation*, vol. 48, no. 5, pp. 728–737, May 2000.

[22] M. E. Yanik and M. Torlak, "Millimeter-wave near-field imaging with two-dimensional SAR data," in *Proc. SRC Techcon*, Austin, TX, USA, Sep. 2018.

[23] D. M. Sheen, D. L. McMakin, and T. E. Hall, "Near-field three-dimensional radar imaging techniques and applications," *Appl. Opt.*, vol. 49, no. 19, pp. E83–E93, Jul. 2010.

[24] J. Fortuny-Guasch and J. M. Lopez-Sanchez, "Extension of the 3-D range migration algorithm to cylindrical and spherical scanning geometries," *IEEE Trans. on Antennas and Propagation*, vol. 49, no. 10, pp. 1434–1444, Oct. 2001.

[25] X. Zhuge and A. G. Yarovoy, "Three-dimensional near-field MIMO array imaging using range migration techniques," *IEEE Trans. on Image Processing*, vol. 21, no. 6, pp. 3026–3033, Jun. 2012.

[26] J. Gao, Y. Qin, B. Deng, H. Wang, and X. Li, "Novel efficient 3D short-range imaging algorithms for a scanning 1D-MIMO array," *IEEE Trans. on Image Processing*, vol. 27, no. 7, pp. 3631–3643, Jul. 2018.

[27] Y. Álvarez, Y. Rodriguez-Vaqueiro, B. Gonzalez-Valdes, F. Las-Heras, and A. García-Pino, "Fourier-based imaging for subsampled multistatic arrays," *IEEE Trans. on Antennas and Propagation*, vol. 64, no. 6, pp. 2557–2562, Jun. 2016.

[28] J. H. G. Ender and J. Klare, "System architectures and algorithms for radar imaging by MIMO-SAR," in *IEEE Radar Conf.*, Pasadena, CA, USA, May 2009, pp. 1–6.

[29] Y. Qi, Y. Wang, W. Tan, and W. Hong, "Application of sparse array and MIMO in near-range microwave imaging," in *Proc. SPIE, SAR Image Analysis, Modeling, and Techniques XI*, vol. 8179, Prague, Czech Republic, Oct. 2011.

[30] L. Qiao, Y. Wang, Z. Zhao, and Z. Chen, "Exact reconstruction for near-field three-dimensional planar millimeter-wave holographic imaging," *Journal of Infrared, Millimeter, and Terahertz Waves*, vol. 36, no. 12, pp. 1221–1236, Dec. 2015.

[31] A. Meta, P. Hoogeboom, and L. P. Ligthart, "Signal processing for FMCW SAR," *IEEE Trans. on Geoscience and Remote Sensing*, vol. 45, no. 11, pp. 3519–3532, Nov. 2007.

[32] G. Wang, J. Muñoz-Ferreras, C. Gu, C. Li, and R. Gómez-García, "Application of linear-frequency-modulated continuous-wave (LFMCW) radars for tracking of vital signs," *IEEE Trans. on Microwave Theory and Techniques*, vol. 62, no. 6, pp. 1387–1399, Jun. 2014.

[33] S. D. Silverstein and Y. Zheng, "Near-field inverse coherent imaging problems: solutions, simulations and applications," in *The 37th Asilomar Conf. on Signals, Systems and Computers*, vol. 1, Pacific Grove, CA, USA, Nov. 2003, pp. 1193–1197.

[34] H. Weyl, "Ausbreitung elektromagnetischer wellen uber einem ebenen leiter," *Ann. Phys*, vol. 365, no. 481, 1919.

[35] L. M. Brekhovskikh and O. A. Godin, *Acoustics of Layered Media II: Point Sources and Bounded Beams*, ser. New York: Springer, 1999.

[36] B. P. Ng, J. P. Lie, M. H. Er, and A. Feng, "A practical simple geometry and gain/phase calibration technique for antenna array processing," *IEEE Trans. on Antennas and Propagation*, vol. 57, no. 7, pp. 1963–1972, Jul. 2009.

[37] C. M. Schmid, C. Pfeffer, R. Feger, and A. Stelzer, "An FMCW MIMO radar calibration and mutual coupling compensation approach," in *European Radar Conf.*, Nuremberg, Germany, Oct. 2013, pp. 13–16.

[38] M. E. Yanik and M. Torlak, "Geolocalization via tracking of wideband radio astronomical sources in the presence of radio frequency interference," in *Proc. IEEE/ION Position, Location and Navigation Symposium*, Monterey, CA, USA, Apr. 2018, pp. 1234–1238.

[39] D. Rife and R. Boorstyn, "Single tone parameter estimation from discrete-time observations," *IEEE Trans. on Information Theory*, vol. 20, no. 5, pp. 591–598, Sep. 1974.

[40] C. E. Cook and M. Bernfield, *Radar Signals: An Introduction to Theory and Application*, ser. New York: Electrical Science Series, 1967.

[41] A. Papoulis, *Systems and Transforms with Applications in Optics*, ser. New York: McGraw-Hill, 1968.

[42] P. T. Gough and D. W. Hawkins, "Imaging algorithms for a strip-map synthetic aperture sonar: minimizing the effects of aperture errors and aperture undersampling," *IEEE Journal of Oceanic Engineering*, vol. 22, no. 1, pp. 27–39, Jan. 1997.

## BIOGRAPHICAL SKETCH

Muhammet Emin Yanik received B.S. and M.S. degrees in electrical and electronics engineering from Hacettepe University in 2007 and 2010, respectively. He is currently pursuing the Ph.D. degree in electrical engineering at the University of Texas at Dallas. He was with Aselsan, Ankara, Turkey, between 2007 and 2016, where he worked on real-time embedded system development for safety-critical avionics applications. His current research focus is on millimeter-wave radars, ultrawideband radar imaging systems, real-time embedded system development, phased array signal processing, and interference mitigation in radio telescopes. He is a Student IEEE member. He is a recipient of Tubitak Graduate Fellowship during 2007-2009, Turkcell Academy Fellowship during 2012-2013, and best poster award at TxACE and Analog/Mixed Signal Circuits Annual Review in 2018.

**CURRICULUM VITAE**

# Muhammet Emin Yanik

April 23, 2019

## Contact Information:

Dept. of Electrical and Computer Eng.
The University of Texas at Dallas
Richardson, TX 75080, U.S.

Phone: (469) 403-9431
Email: muhammet.yanik@utdallas.edu
Web: linkedin.com/in/muhammet-emin-yanik/

## Educational History:

B.S., Electrical and Electronics Engineering, Hacettepe University, 2007
M.S., Electrical and Electronics Engineering, Hacettepe University, 2010

*Effects of correlation and antenna polarization on the MIMO system performance*
M.S. Thesis, Advisor: Dr. Mehmet Safak

*Line and circle detection in 2D colored images by using Hough transformation*
B.S. Design Project, Advisor: Dr. Yakup Ozkazanc

## Employment History:

Systems Engineering Intern, Texas Instruments, February 2019 – Present
Research Assistant, The University of Texas at Dallas, August 2016 – January 2019
Co-Founder and Team Leader, Sidus Innovations, March 2016 – Present
Senior Embedded Systems Engineer, Aselsan, June 2007 – July 2016

## Professional Recognitions and Honors:

Winner of the Spirit of Innovation Technology Competition, USICOC, Nov. 2018
Best Poster Award, Semiconductor Research Corporation and TxACE, Oct. 2018
Young Entrepreneur Program Award, TUBITAK, Mar. 2016
Outstanding Young Engineer Award, Turkish Future Fighter Program, Sep.2015
TURKCELL Academy Graduate Fellowship, Sep. 2012
TUBITAK Graduate Fellowship, Sep. 2007
Honor student by ranking 4th among B.S. graduates, Hacettepe University, Jun. 2007
Top 0.1% in the Nationwide University Entrance Exam among 1.5M candidates, Jun. 2002

## Publications:

[J1] **M.E. Yanik** and M. Torlak, "Near-Field MIMO-SAR Millimeter-Wave Imaging With Sparsely Sampled Aperture Data," in IEEE Access, vol. 7, pp. 31801-31819, Mar. 2019

[C1] **M.E. Yanik** and M. Torlak, Near-field two-dimensional SAR imaging by millimeter-wave radar for concealed item detection, IEEE Radio & Wireless Symposium, Orlando, Florida, US, Jan. 2019.
[C2] **M.E. Yanik** and M. Torlak, Millimeter-wave near-field imaging with two-dimensional SAR data, Proc. SRC Techcon, Austin, Texas, US, Sep. 2018.
[C3] **M.E. Yanik** and M. Torlak, Geolocalization via tracking of wideband radio astronomical sources in the presence of radio frequency interference, IEEE/ION Position Location and Navigation Symposium, Monterey, California, US, Apr. 2018.
[C4] S.A. Yildirim, M. Safak and **M.E. Yanik**, Diversity loss-array gain tradeoff in doubly correlated MIMO beamforming systems, 2010 IEEE 18th Signal Processing and Communications Applications Conference, Diyarbakir, Turkey, Apr. 2010.

## Skills:

Programming Languages: MATLAB, C/C++, CUDA, Java, Python, UML, SysML
Operating System: Linux (Ubuntu), FreeRTOS, ROS, MS Windows, MacOS
IDE: Visual Studio, Code Composer Studio, Eclipse, Arduino, Android Studio, Qt
Engineering Tools: LabView, Github, Simulink, Autodesk Inventor, KiCAD, Doors, Rhapsody, Thingspeak, MATLAB Mobile, MS Office, Unity 3D

## Professional Memberships:

Institute of Electrical and Electronics Engineers (IEEE), 2017–present